

**Effects of internal structural parameters on the properties of Ba-substituted  $\text{La}_{0.5}\text{Sr}_{0.5}\text{MnO}_3$** O. Chmaissem,<sup>1,2</sup> B. Dabrowski,<sup>1,2</sup> S. Kolesnik,<sup>1</sup> J. Mais,<sup>1</sup> L. Suescun,<sup>1,2</sup> and J. D. Jorgensen<sup>2,\*</sup><sup>1</sup>*Physics Department, Northern Illinois University, DeKalb, Illinois 60115, USA*<sup>2</sup>*Materials Science Division, Argonne National Laboratory, Argonne, Illinois 60439, USA*

(Received 25 May 2006; revised manuscript received 8 September 2006; published 20 October 2006)

A series of barium substituted  $\text{La}_{0.5}\text{Sr}_{0.5-x}\text{Ba}_x\text{MnO}_3$  materials has been synthesized and investigated using neutron powder diffraction. We show that Ba substitution suppresses the low-temperature orbital ordering that has been previously observed in  $\text{La}_{0.5}\text{Sr}_{0.5}\text{MnO}_3$ , and demonstrate the evolution of the magnetic and nuclear structures as a function of increasing Ba content. All our samples exhibit paramagnetic and ferromagnetic properties near room temperature with the ferromagnetic structures described as  $I4/mc'm'$  and  $P4/mn'm'$  for  $x=0, 0.1, \text{ and } 0.2$  and  $x=0.3, 0.4, \text{ and } 0.5$ , respectively. The Mn magnetic moments align ferromagnetically in the direction of the  $c$  axis with no evidence for any spin canting. The effects of A-site ionic size, size variance, and strains in the lattice on the ferromagnetic ordering temperature,  $T_C$ , are discussed and compared with other members of the general  $\text{La}_{0.5}(\text{Ca}, \text{Sr}, \text{Ba})_{0.5}\text{MnO}_3$  series. Depending on the substitution path, the relationship between  $T_C$  and  $\langle r_A \rangle$  is either near constant or looks like an inverted parabola. Finally, details of the magnetic, resistive, structural, and interatomic properties are presented.

DOI: [10.1103/PhysRevB.74.144415](https://doi.org/10.1103/PhysRevB.74.144415)

PACS number(s): 75.25.+z, 61.12.-q, 75.30.-m, 75.50.Dd

**INTRODUCTION**

Perovskite-based manganites have recently been at the center of intense research because of their colossal magnetoresistive properties and charge and/or orbital ordering in compositions with particular  $\text{Mn}^{3+}$ :  $\text{Mn}^{4+}$  ratios (e.g., 1:1, 1:2, etc). In  $\text{La}_{0.5}\text{Ca}_{0.5}(\text{Mn}_{0.5}^{3+}\text{Mn}_{0.5}^{4+})\text{O}_3$ ,<sup>1</sup> for example, a ratio of 1:1 results in a zigzaglike charge distribution of the  $\text{Mn}^{3+}$  and  $\text{Mn}^{4+}$  ions and charge ordering of the charge-exchanged (CE) type. A ratio of 1:1 is usually achieved by the substitution of a divalent alkaline element such as Ca, Sr, or Ba for half the trivalent A-site ions in  $\text{AMnO}_3$  (e.g., where  $A=\text{La}$  or other rare earth elements). As such,  $\text{La}_{0.5}\text{Ca}_{0.5}\text{MnO}_3$ ,  $\text{La}_{0.5}\text{Sr}_{0.5}\text{MnO}_3$ , and  $\text{La}_{0.5}\text{Ba}_{0.5}\text{MnO}_3$  have been synthesized and shown to exhibit significantly different magnetic and structural properties because of the size effect of the substituting element and the ionic size variance  $\sigma^2$  (defined as the variance of sizes between different ions occupying the same A-site).<sup>2-4</sup>  $\text{La}_{0.5}\text{Ca}_{0.5}\text{MnO}_3$  (Refs. 5 and 6) can be easily synthesized under ambient conditions; however,  $\text{La}_{0.5}\text{Sr}_{0.5}\text{MnO}_3$  and  $\text{La}_{0.5}\text{Ba}_{0.5}\text{MnO}_3$  may form only under stringent and well-controlled conditions.<sup>7,8</sup> For  $\text{La}_{0.5}\text{Ca}_{0.5}\text{MnO}_3$ , charge ordering, ferromagnetic, and antiferromagnetic properties have all been reported to take place at different temperatures below 300 K.<sup>1</sup> In the case of  $\text{La}_{0.5}\text{Sr}_{0.5}\text{MnO}_3$ , a ferromagnetic phase coexists with an A-type orbitally ordered antiferromagnetic phase over a wide temperature range below  $\sim 200$  K with no evidence for any charge ordering.<sup>7</sup> As for  $\text{La}_{0.5}\text{Ba}_{0.5}\text{MnO}_3$ , only ferromagnetic properties have been observed and reported.

The goal of this paper is to investigate the effects of increasing the average size of the A-site ions on the magnetic and structural properties of Ba-substituted  $\text{La}_{0.5}\text{Sr}_{0.5}\text{MnO}_3$ . The isoivalent substitution of Ba (or Ca) for Sr preserves the average charge at both the A- and B-sites (i.e.,  $\text{La}_{0.5}\text{Sr}_{0.5-x}\text{Ba}_x$  and Mn sites, respectively). In this paper, we demonstrate that the replacement of small amounts of  $\text{Sr}^{2+}$  by  $\text{Ba}^{2+}$  in  $\text{La}_{0.5}\text{Sr}_{0.5}\text{MnO}_3$  results in the suppression of the

previously observed low-temperature phase separation and the orbitally ordered antiferromagnetic phase.<sup>7</sup> For all members of the  $\text{La}_{0.5}\text{Sr}_{0.5-x}\text{Ba}_x\text{MnO}_3$  series, the samples exhibit ferromagnetic properties with a Curie temperature,  $T_C$ , decreasing as a function of increasing Ba content. A similarly decreasing  $T_C$  has previously been observed in  $\text{La}_{0.6}\text{Sr}_{0.4-x}\text{Ba}_x\text{MnO}_3$ ,<sup>9,10</sup>  $\text{Pr}_{0.5}\text{Sr}_{0.5-x}\text{Ba}_x\text{MnO}_3$ ,<sup>11,12</sup> and  $\text{Nd}_{0.7}\text{Sr}_{0.3-x}\text{Ba}_x\text{MnO}_3$ ,<sup>13</sup> for example, and interpreted in terms of increasing ionic size variance  $\sigma^2$  (Ref. 9) or increasing Mn-O bond lengths.<sup>10</sup> Both of these arguments mainly relied on Shannon's tabulated ionic sizes<sup>14</sup> that differ appreciably, as we have previously shown,<sup>4,7,15,16</sup> from the observed real values for manganites. Here, we use neutron diffraction to measure the relevant bond lengths and bond angles and show that the explanation of  $T_C$  behavior only in terms of ionic sizes and ionic size variance is not sufficient, especially in the regime where structural distortions from the cubic phase are very small. We combine our results with data published in the literature for  $\text{La}_{0.5}\text{Ca}_{0.5-x}\text{Sr}_x\text{MnO}_3$  and show the behavior of  $T_C$  as a function of increased average ionic size radius. We explain the  $T_C$  behavior in terms of ionic size, ionic size variance, local structural distortions, and strains in the lattice. Finally, we discuss the effects of interatomic  $\langle \text{Mn-O} \rangle$  bond lengths in A-site disordered  $\text{La}_{0.5}\text{Ba}_{0.5}\text{MnO}_3$  and A-site ordered  $\text{LaBaMn}_2\text{O}_6$  (Ref. 17) on the observed  $T_C$  enhancement for the latter phase.

**MATERIALS SYNTHESIS AND CHARACTERIZATION**

Single phase Ba-substituted  $\text{La}_{0.5}\text{Sr}_{0.5}\text{MnO}_3$  materials have been synthesized using a well-controlled two-step solid state reaction method. Raw  $\text{La}_2\text{O}_3$ ,  $\text{MnO}_2$ ,  $\text{SrCO}_3$ , and  $\text{BaCO}_3$  powders were thoroughly mixed in stoichiometric amounts after drying  $\text{La}_2\text{O}_3$  in air at 900 °C. The precursor mixtures were repeatedly ground and fired in air up to 1200 °C, then in flowing argon (99.999%) up to the final synthesis temperature. The final synthesis temperature was varied from 1420 to 1440 °C with increasing Ba content and

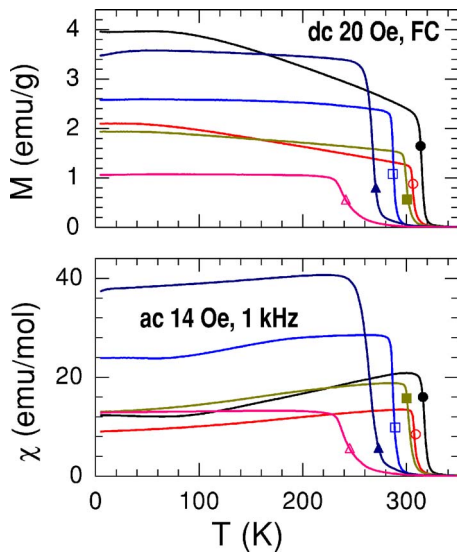


FIG. 1. (Color online) dc and ac magnetic measurements at 20 Oe and 14 Oe/1 kHz, respectively. These measurements were used to extract the  $T_C$  values reported in this paper. Closed circles ( $x=0$ ), open circles ( $x=0.1$ ), closed squares ( $x=0.2$ ), open squares ( $x=0.3$ ), closed triangles ( $x=0.4$ ), and open triangles ( $x=0.5$ ).

resulted in single-phase oxygen deficient perovskites. Fully oxygenated samples were obtained by annealing the deficient materials in air at 500 °C followed by slow cooling to room temperature. A few hundred milligrams of each sample were decomposed in a high-temperature Thermogravimetric Analysis system (Thermo-Cahn TGA-171) to confirm the exact oxygen stoichiometry of the material within the accuracy of our measurement system (better than  $\pm 0.005$  oxygen atoms per unit cell).

A Quantum Design Physical Properties Measurement System Model 6000 was used for the characterization of the resistive and magnetic properties of the materials. The ferromagnetic transition temperatures,  $T_C$ 's, reported in this paper were extracted from our dc and ac magnetic measurements performed in external magnetic fields of 20 Oe and 14 Oe/1 kHz, respectively. The phase formation, purity, and crystalline properties of the samples were checked and monitored by x-ray powder diffraction. Several samples were selected for detailed temperature-dependent structural investigations using neutron powder diffraction (NPD).

Time-of-flight neutron powder diffraction data were collected on the special environment powder diffractometer (SEPD)<sup>18</sup> at the intense pulsed neutron source (IPNS). Diffraction data were acquired at several temperatures between 40 and 500 K using a closed-cycle helium refrigerator with heating capabilities above room temperature. High-resolution backscattering data, from 0.5 to 4 Å  $d$  spacing, and medium resolution data, 1 to 10 Å  $d$  spacing, were analyzed with the Rietveld analysis method used in the General Structure Analysis System (GSAS) code.<sup>19,20</sup> The medium resolution data banks (histogram #2) were particularly useful below the magnetic transition temperatures of the materials because they contain several magnetic peaks of significant intensities. In the analysis, background, peak width, and extinction parameters were refined, together with the lattice

parameters, atomic positions, and isotropic and anisotropic temperature factors for the cations and oxygen atoms, respectively.

## RESULTS

### Magnetic and resistive properties

The particular importance of  $\text{La}_{0.5}\text{Sr}_{0.5}\text{MnO}_3$  lies in its location on a steep boundary line on the phase diagram between two significantly different structural regions.<sup>7</sup> At low temperatures, a large part of the material undergoes a simultaneous ferromagnetic tetragonal to antiferromagnetic orthorhombic structural and magnetic phase transition; however, the bulk material remains metallic because of the metallic properties of the remaining ferromagnetic phase.

Over the last few years, the resistive and magnetic behaviors of many colossal magnetoresistance (CMR) materials have been shown to be significantly affected by the slightest disturbance of a delicate charge balance at the Mn sites. For example, in  $\text{La}_{0.5}\text{Sr}_{0.5}\text{Mn}^{(3.5+)}\text{O}_3$ , charge imbalance may be achieved by either decreasing or increasing the Sr content resulting in rhombohedral ferromagnetic or tetragonal ferromagnetic and orbital-ordered antiferromagnetic phases, respectively.<sup>7</sup> In other studies, the A-site size effects on the magnetic and transport properties of the material have been demonstrated even when the charge balance has not been disturbed. For example, the isovalent substitution of  $\text{Ca}^{2+}$  for  $\text{Sr}^{2+}$  in  $\text{La}_{1-x}\text{Sr}_x\text{MnO}_3$  has been shown to result in new magnetic and resistive properties.<sup>11,21</sup> Similarly, we expect that the materials' behavior will change by increasing the average

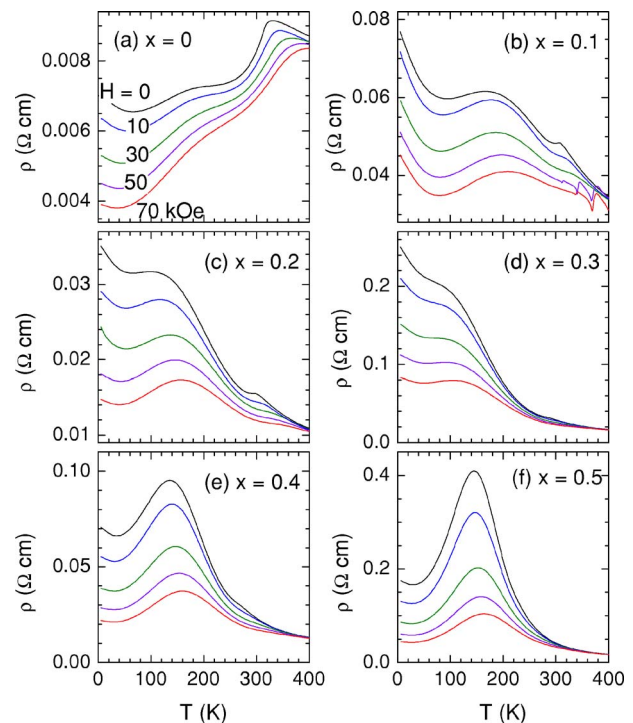


FIG. 2. (Color online) Resistivity measurements for  $\text{La}_{0.5}\text{Sr}_{0.5-x}\text{Ba}_x\text{MnO}_3$  as a function of external magnetic fields. Large magnetoresistive behavior is observed for all the samples.

TABLE I. Structural parameters for  $\text{La}_{0.5}\text{Sr}_{0.4}\text{Ba}_{0.1}\text{MnO}_3$  and  $\text{La}_{0.5}\text{Sr}_{0.3}\text{Ba}_{0.2}\text{MnO}_3$  at 380 K and 40 K. Refinements carried out using the tetragonal  $I4/mcm$  space group. La, Sr, and Ba site occupancies fixed at their nominal values. Thermal factors for La, Sr, and Ba constrained to be equal.

Sample	Atom position	Anisotropic thermal factors	$\text{La}_{0.5}\text{Sr}_{0.4}\text{Ba}_{0.1}\text{MnO}_3$		$\text{La}_{0.5}\text{Sr}_{0.3}\text{Ba}_{0.2}\text{MnO}_3$	
			380	52.5	380	40
$T$ (K)						
			$I4/mcm$	$I4/mcm$	$I4/mcm$	$I4/mcm$
$a$ (Å)			5.47331(4)	5.45227(3)	5.48755(3)	5.47036(2)
$c$ (Å)			7.7549(1)	7.7576(1)	7.77156(9)	7.76533(7)
$V$ (Å <sup>3</sup> )			232.315(6)	230.612(6)	234.026(5)	232.377(4)
La,Ba,Sr	$(\frac{1}{2} 0 \frac{1}{4})$	$100 \times U_{\text{iso}}$ (Å <sup>2</sup> )	0.86(4)	0.43(3)	0.83(3)	0.34(2)
Mn	(0 0 0)	$100 \times U_{\text{iso}}$ (Å <sup>2</sup> )	0.74(5)	0.34(4)	0.55(4)	0.22(3)
		$\mu_z$ ( $\mu_B$ )	0.2(2)	3.54(3)	0.14(10)	3.51(3)
$\text{O}_{\text{apical}}$	$(0 0 \frac{1}{4})$	$100 \times (U_{11}=U_{22})$ (Å <sup>2</sup> )	1.7(1)	0.93(6)	1.9(3)	0.90(5)
		$100 \times U_{33}$ (Å <sup>2</sup> )	1.5(3)	0.8(1)	1.4(4)	0.6(1)
$\text{O}_{\text{equatorial}}$	$(x x + \frac{1}{2} 0)$	$x$	0.2669(3)	0.2719(2)	0.2598(4)	0.2671(1)
		$100 \times (U_{11}=U_{22})$ (Å <sup>2</sup> )	1.37(8)	0.75(4)	1.5(1)	0.77(3)
		$100 \times U_{33}$ (Å <sup>2</sup> )	2.0(2)	1.05(8)	1.7(2)	1.05(7)
		$100 \times U_{12}$ (Å <sup>2</sup> )	0.7(1)	0.41(6)	0.6(2)	0.37(5)
$R_P$ (%)			8.80	9.17	7.80	6.21
$R_{WP}$ (%)			12.83	13.56	12.34	9.64
$\chi^2$			1.193	1.266	1.112	1.569
Mn- $\text{O}_{\text{apical}}$			1.93873(3)	1.93939(2)	1.94289(2)	1.94133(2)
Mn- $\text{O}_{\text{equatorial}}$			1.93954(14)	1.93509(12)	1.94164(11)	1.93857(8)
Mn- $\text{O}_{\text{apical}}$ -Mn			180	180	180	180
Mn- $\text{O}_{\text{equatorial}}$ -Mn			172.27(12)	169.97(8)	175.51(17)	172.19(7)

ionic size of the A-site through the isovalent substitution of  $\text{Ba}^{2+}$  for  $\text{Sr}^{2+}$ .

As shown in Fig. 1, all of our Ba-substituted  $\text{La}_{0.5}\text{Sr}_{0.5-x}\text{Ba}_x\text{MnO}_3$  samples exhibit ferromagnetic properties with the  $T_C$  slowly decreasing upon increasing the Ba content and then decreasing at a faster rate when approaching the end member  $\text{La}_{0.5}\text{Ba}_{0.5}\text{MnO}_3$  of the phase diagram. Magnetic measurements at 70 kOe fields show consistent saturation values of  $\sim 3.3$  to  $3.5\mu_B$  in good agreement with the expected value of  $3.5\mu_B$  for a  $\text{Mn}^{3+}:\text{Mn}^{4+}$  ratio of 1:1.

Resistivity measurements performed in external magnetic fields up to 70 kOe are displayed in Fig. 2. The figure shows anomaly kinks that correspond to the materials' ferromagnetic transition temperatures,  $T_C$ 's, followed at lower temperatures by broad metal-to-insulator (MI) type transition humps. The presence of similar MI humps has previously been attributed to granular or grain boundary effects in other materials with similar compositions.<sup>8,21-26</sup> Other studies demonstrated that similar properties can be produced by introducing some oxygen vacancies in the material or by significantly changing the synthesis and sintering conditions.<sup>27-29</sup>

Resistivity measurements carried out in air at temperatures up to 1000 °C showed an irreversible behavior with the resistivity decreasing when the temperature increases above  $\sim 600$  °C. X-ray diffraction patterns showed the samples to decompose at temperatures above 550–600 °C (data not shown). The decomposed samples contain small amounts of

hexagonal  $\text{BaMnO}_3$  in addition to the main perovskite phase. The presence of the impurity  $\text{BaMnO}_3$  phase has frequently been observed in  $\text{La}_{0.5}\text{Sr}_{0.5-x}\text{Ba}_x\text{MnO}_3$  samples with Ba contents  $x \geq 0.3$ . The significantly increased ferromagnetic transition temperature for the decomposed  $x=0.5$  sample indicates the decomposition of the materials to  $\text{BaMnO}_3$  plus a composition with  $x < 0.5$  in agreement with the results of the synthesis conditions. In another study, Raman spectroscopy demonstrated the presence of trace amounts of  $\text{BaMnO}_3$  in a  $\text{La}_{1-x}\text{Ba}_x\text{MnO}_3$  sample that appeared to be single phase using x-ray diffraction.<sup>30</sup> Therefore, the presence of  $\text{BaMnO}_3$  in the form of nanoparticles or a grain boundary phase with dimensions below the diffraction coherent scattering length is possible and could explain the observed humps in our resistivity data and the strong dependence on magnetic field.

### Neutron powder diffraction

As described above,  $\text{La}_{0.5}\text{Sr}_{0.5}\text{MnO}_3$  exhibits a series of nuclear and magnetic phase transitions with the material changing from paramagnetic to ferromagnetic to antiferromagnetic (AFM) at  $\sim 320$  K and  $\sim 190$  K, respectively.<sup>7</sup> The paramagnetic and ferromagnetic phases crystallize in a tetragonal structure of space group  $I4/mcm$ , while the orbital-ordered A-type antiferromagnetic phase is best described using the symmetry of the orthorhombic  $Fmmm$  space group.

For Ba-substituted  $\text{La}_{0.5}\text{Sr}_{0.5-x}\text{Ba}_x\text{MnO}_3$  materials, our neutron powder diffraction patterns clearly show the sup-

TABLE II. Structural parameters for  $\text{La}_{0.5}\text{Sr}_{0.5-x}\text{Ba}_x\text{MnO}_3$  ( $x=0.3, 0.4,$  and  $0.5$ ) in the cubic  $Pm\bar{3}m$  and tetragonal  $P4/mmm$  space groups. La, Sr, and Ba site occupancies fixed at their nominal values. Thermal factors for La, Sr, and Ba constrained to be equal.

$T$ (K)	Atom position	Anisotropic thermal factors	$\text{La}_{0.5}\text{Sr}_{0.2}\text{Ba}_{0.3}\text{MnO}_3$	$\text{La}_{0.5}\text{Sr}_{0.1}\text{Ba}_{0.4}\text{MnO}_3$			$\text{La}_{0.5}\text{Ba}_{0.5}\text{MnO}_3$		
			293 K	294.5 K	50 K	295 K	200 K	100 K	10 K
			$P4/mmm$	$Pm\bar{3}m$	$P4/mmm$	$Pm\bar{3}m$	$P4/mmm$	$P4/mmm$	$P4/mmm$
$a$ (Å)			3.88948(2)	3.89819(2)	3.88947(2)	3.90878(2)	3.9033(1)	3.89935(8)	3.89841(6)
$c$ (Å)			3.89267(2)		3.89173(2)		3.9072(3)	3.9053(2)	3.9046(2)
$V$ (Å <sup>3</sup> )			58.889(1)	59.237(1)	58.874(1)	59.720(1)	59.529(1)	59.380(1)	59.341(1)
La, Sr, Ba	$(\frac{1}{2} \frac{1}{2} 0)$	$100 \times U_{\text{iso}}$ (Å <sup>2</sup> )	0.71(2)	0.93(3)	0.58(2)	0.68(3)	0.52(3)	0.34(3)	0.33(2)
Mn	$(0 0 0)$	$100 \times U_{\text{iso}}$ (Å <sup>2</sup> )	0.49(3)	0.68(3)	0.44(3)	0.35(4)	0.40(5)	0.26(4)	0.27(2)
		$\mu_Z$ ( $\mu_B$ )	0.5(1)		3.38(4)		2.79(9)	3.30(9)	3.53(5)
$\text{O}_{\text{apical}}$	$(0 0 \frac{1}{2})$	$100 \times U_{11} =$ $100 \times U_{22}$ (Å <sup>2</sup> )	1.9(4)	2.08(4)	1.5(4)	1.78(5)	2.3(3)	1.4(3)	0.6(1)
		$100 \times U_{33}$ (Å <sup>2</sup> )	1.1(4)	1.30(6)	1.3(4)	0.91(7)	1.1(5)	1.3(4)	1.1(2)
$\text{O}_{\text{equa.}}$	$(\frac{1}{2} 0 0)$	$100 \times U_{11}$ (Å <sup>2</sup> )	0.9(2)		0.5(2)		0.5(2)	0.3(1)	0.1(1)
		$100 \times U_{22}$ (Å <sup>2</sup> )	1.4(4)		1.1(3)		0.7(2)	0.8(3)	1.9(2)
		$100 \times U_{33}$ (Å <sup>2</sup> )	2.3(3)		2.2(3)		2.1(3)	1.8(2)	1.7(2)
$R_P$ (%)			6.4	6.71	7.16	5.92	6.07	5.79	5.33
$R_{WP}$ (%)			9.83	10.19	10.39	9.27	9.56	8.90	7.76
$\chi^2$			1.422	1.377	1.756	1.205	1.219	1.368	1.561
Mn- $\text{O}_{\text{apical}}$	$\times 2$		1.94634(1)	1.94910(1)	1.94586(1)	1.95439(1)	1.9536(1)	1.95266(8)	1.95230(7)
Mn- $\text{O}_{\text{equa.}}$	$\times 4$		1.94474(1)	1.94910(1)	1.94473(1)	1.95439(1)	1.95164(6)	1.94967(4)	1.94921(3)

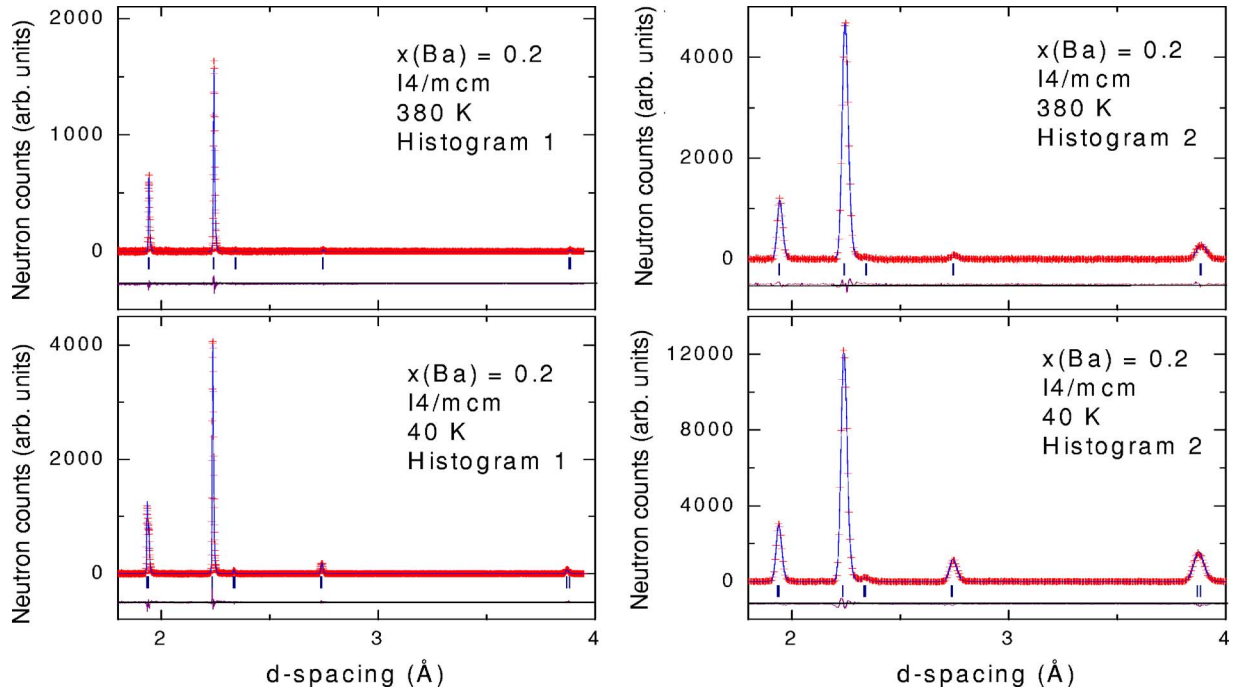


FIG. 3. (Color online) Best-fit Rietveld refinement for  $\text{La}_{0.5}\text{Sr}_{0.3}\text{Ba}_{0.2}\text{MnO}_3$  in the 1.8–4 Å  $d$ -spacing range showing observed (+) and calculated intensities (solid line) at 380 K (upper panels) and 40 K (lower panels). The backscattering (histogram 1) and the 90° (histogram 2) databanks were used in the refinements. Tick marks below the patterns show the positions of the nuclear and magnetic Bragg peaks. The difference between observed and calculated intensities is shown below the tick marks.

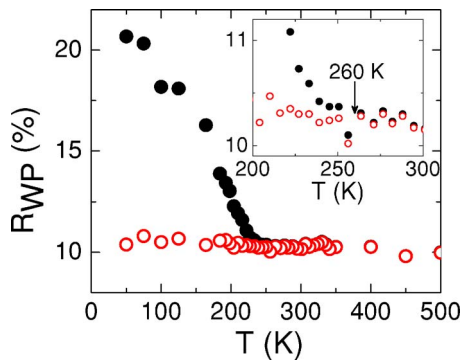


FIG. 4. (Color online)  $\text{La}_{0.6}\text{Sr}_{0.1}\text{Ba}_{0.4}\text{MnO}_3$ : Weighted profile residual agreement factor obtained from refinements using cubic  $Pm\bar{3}m$  (filled circles) and tetragonal  $P4/mmm'$  (open circles) space groups. Significantly improved refinements are obtained using the tetragonal magnetic symmetry below  $T_C$ .

pression of the low temperature orbital-ordered AFM phase and the retention of the tetragonal  $I4/mcm$  symmetry for all samples with  $x \leq 0.3$ . We observe this tetragonal structure at all measured temperatures above and below  $T_C$  for  $x=0.1$  and 0.2. For the  $x=0.3$  material, we observe a simultaneous structural phase transition from cubic  $Pm\bar{3}m$  to tetragonal  $I4/mcm$  occurring at  $T_C$ . In  $I4/mcm$ , the  $\text{MnO}_6$  octahedra are free to rotate around the  $c$  axis and the ferromagnetic alignment of the Mn moments is achievable only in the direction of the  $c$  axis with no spin canting being allowed that could result in any in-plane ferromagnetic or antiferromagnetic component (because of the tetragonal fourfold symmetry axes). Canting that would result in an in-plane antiferromagnetic component, may only be possible using a lower structural symmetry [such as the previously reported  $Imma$  symmetry for  $\text{La}_{0.7}\text{Ba}_{0.3}\text{MnO}_3$  (Ref. 31)] and extra antiferromagnetic reflections should become visible. The absence of antiferromagnetic peaks in our diffraction patterns clearly indicates the ferromagnetic alignment of the Mn moments in the direction of the  $c$  axis. In this work, we determine the ferromagnetic symmetry to be  $I4/mc'm'$  for all compositions with  $x \leq 0.3$  by taking the time reversal symmetry of the mirrors perpendicular to the  $\langle 100 \rangle$  and  $\langle 110 \rangle$  directions. Select structural parameters and bond lengths are listed in Tables I and II. Best-fit Rietveld refinement patterns for  $\text{La}_{0.5}\text{Sr}_{0.3}\text{Ba}_{0.2}\text{MnO}_3$  are displayed in Fig. 3.

With the further increase of Ba content, larger A-site ionic size averages are obtained together with stretched Mn-O bonds and straighter in-plane Mn-O-Mn bond angles. Thus, higher symmetry structures result in which the  $\text{MnO}_6$  octahedral rotations are completely suppressed. The structures of the  $x=0.4$  and 0.5 samples were refined using the cubic  $Pm\bar{3}m$  and tetragonal  $P4/mmm$  (a subgroup of  $Pm\bar{3}m$ , see Fig. 4) symmetries at all temperatures above and below  $T_C$ , respectively. In the refinements, the “pseudocubic/tetragonal” unit cell is required to eliminate the inconsistency between the ferromagnetic behavior of the materials and the threefold symmetry of the cubic  $Pm\bar{3}m$  space group.<sup>28,32,33</sup> In Fig. 5, we display two best-fit Rietveld refinement models at 10 K in which the subtle discrepancies

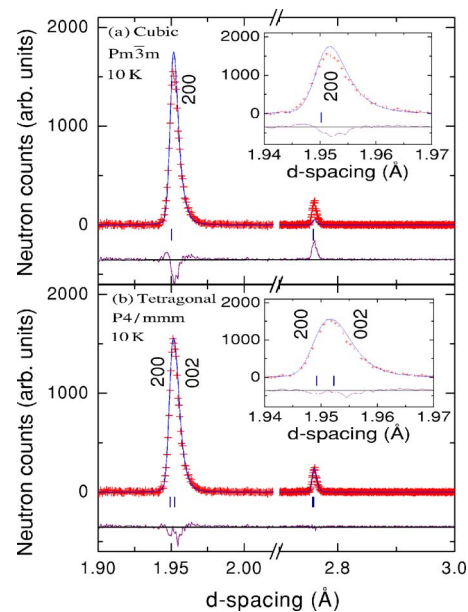


FIG. 5. (Color online) Portions of best-fit Rietveld patterns for  $\text{La}_{0.5}\text{Ba}_{0.5}\text{MnO}_3$  from refinements using cubic  $Pm\bar{3}m$  (a) and tetragonal  $P4/mmm$  (b) symmetries. The ferromagnetic peaks may only be fit using the tetragonal magnetic  $P4/mmm'$  symmetry (see text for more details).

between observed and calculated intensities (using  $Pm\bar{3}m$ ) are completely accounted for using  $P4/mmm$  (see the 200 reflection, for example) in addition to the detection of several significant ferromagnetic intensities growing on top of some nuclear peaks—most noticeably on the 110 reflection at  $\sim 2.75 \text{ \AA}$ . In  $P4/mmm$ , the ferromagnetic easy axis ( $c$  axis) is slightly longer than the basal  $a$  axis [for example,  $a = 3.89841(6) \text{ \AA}$  and  $c = 3.9046(1) \text{ \AA}$  for  $x=0.3$ ] and the ferromagnetic alignment of the Mn moments is allowed by taking the time reversal symmetry of the mirrors perpendicular to the  $\langle 100 \rangle$  and  $\langle 110 \rangle$  directions, thus resulting in the magnetic space group  $P4/mmm'$ .

Finally, refinements of the structure at the lowest measured temperatures yielded magnetic moments of  $3.55(3)\mu_B$ ,  $3.51(3)\mu_B$ ,  $3.62(3)\mu_B$ ,  $3.53(5)\mu_B$ , and  $3.51(5)\mu_B$  for  $x=0.1$ , 0.2, 0.3, 0.4, and 0.5, respectively, in good agreement with the expected value for the  $\text{Mn}^{(3.5+)}$  magnetic moments.

## DISCUSSION

### Structural properties

Evolution of the room temperature lattice parameters, reduced unit cell volume, Mn-O bond lengths, and Mn-O-Mn bond angles is displayed in Fig. 6 as a function of increasing Ba content. As shown in the figure, the formation of a continuous solid solution is demonstrated by the linear behavior of the measured unit cell volume and the smooth structural transition from tetragonal to cubic at  $x \sim 0.3$ . The similarity between the Mn-O bond lengths and lattice parameters indicates the gradual suppression of the  $\text{MnO}_6$  octahedral distortion with increasing Ba content. The buckled in-plane Mn

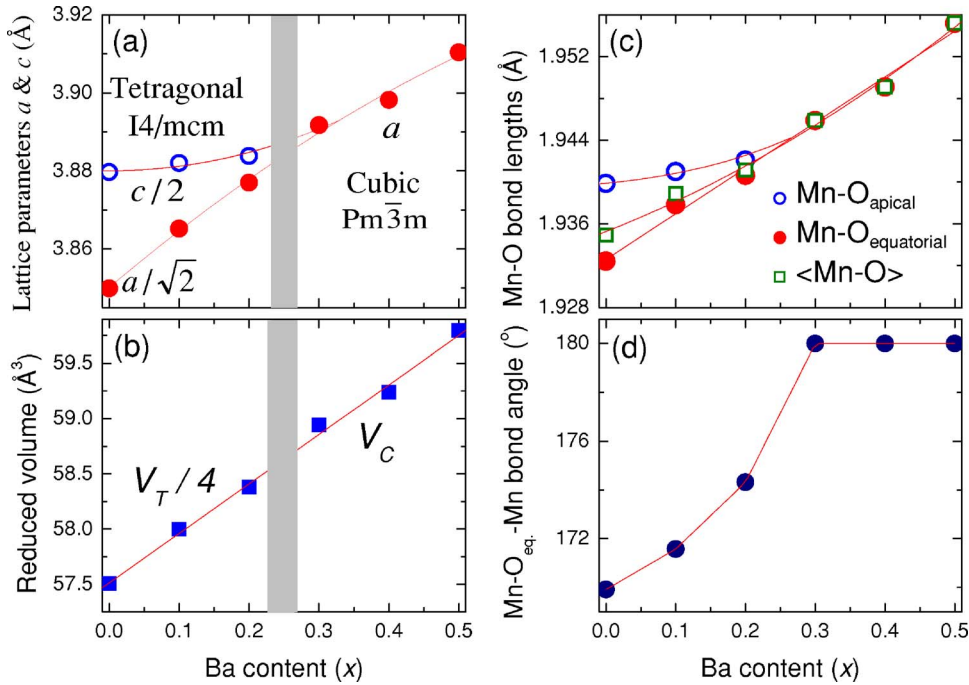


FIG. 6. (Color online) (a) Room-temperature lattice parameters, (b) reduced unit cell volume (per one chemical formula),  $V_T$  and  $V_C$  refer to tetragonal and cubic unit cell volumes, respectively, (c) Mn-O bonds, and (d) equatorial Mn-O-Mn bond angles for all members of the  $\text{La}_{0.5}\text{Sr}_{0.5-x}\text{Ba}_x\text{MnO}_3$  series. The formation of a solid solution is demonstrated by the continuous linear increase of the unit cell volume as a function of increasing Ba content.

$-\text{O}_{\text{eq}}$ -Mn bond angle increases from  $\sim 171^\circ$  for  $x=0$  to straight  $180^\circ$  for  $x \sim 0.3$ .

Temperature-dependent properties of the lattice parameters are displayed in Fig. 7 for all members of the  $\text{La}_{0.5}\text{Sr}_{0.5-x}\text{Ba}_x\text{MnO}_3$  series. We note here the similarity in lattice behavior for the  $x=0.1$  sample and the ferromagnetic

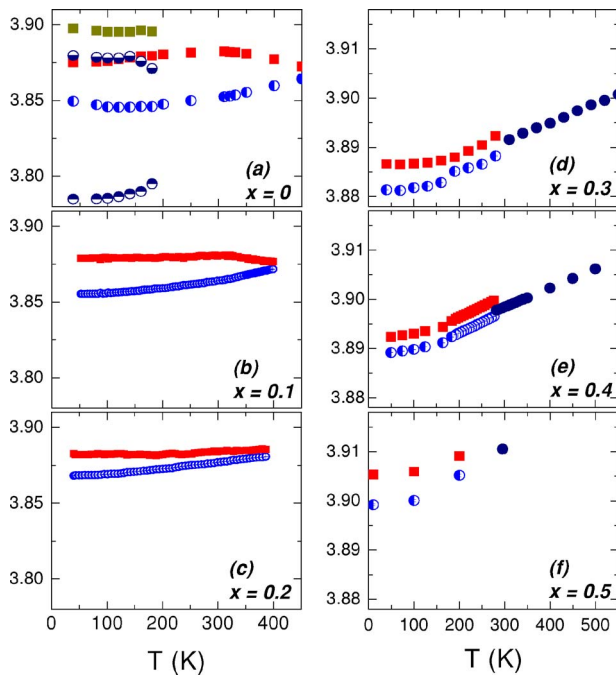


FIG. 7. (Color online) Temperature dependence of the reduced lattice parameters  $a$  (circles) and  $c$  (squares) [ $a/\sqrt{2}$ ,  $c/2$  for  $x=0$ , 0.1, and 0.2] for all members of the  $\text{La}_{0.5}\text{Sr}_{0.5-x}\text{Ba}_x\text{MnO}_3$  series. For  $x=0$ , the lattice parameters  $a$  (half-up filled circles),  $b$  (half-down filled circles), and  $c$  (squares) of the low-temperature antiferromagnetic phase are also shown.

phase of the unsubstituted  $x=0$  sample. For both samples, the  $c$  axes exhibit negative thermal expansion upon decreasing temperature to reach a maximum near the onset of ferromagnetic ordering before reversing sign to slowly decrease with further temperature drops. For the  $x=0.2$  sample, a quite different behavior is observed for the  $c$  axis showing no significant response around  $T_C$  ( $\sim 300$  K) and remaining essentially constant at all temperatures below  $\sim 240$  K. For the three remaining samples, the  $a$ - and  $c$ -lattice parameter curves continue to shift to higher magnitudes with increasing Ba while the difference between the two parameters decreases until reaching zero for the cubic structure, see Figs. 7(d)–7(f). Figure 8(a) shows the unit cell volume regularly increasing in magnitude as a function of increasing temperature and Ba content. As mentioned above, this increased volume relates to larger average A-site ionic sizes that results in stretching the equatorial Mn-O-Mn bond angles to become perfectly straight when in the cubic regime, see Fig. 8(b).

Because of the high-symmetry positions of Mn and  $\text{O}_{\text{apical}}$  atoms in  $I4/mcm$ ,  $P4/mmm$ , and  $Pm\bar{3}m$ , the  $c$  axis and apical Mn-O bonds exhibit identical behaviors over the full measured temperature range, see Figs. 7 and 9. As shown in Fig. 9, the equatorial and apical Mn-O bonds continuously shift upward and the bond divergence (octahedral distortion) diminishes significantly upon increasing temperature and Ba content. It is interesting to note that upon warming, the apical and equatorial Mn-O bonds for the  $x=0$  and  $x=0.1$  samples intersect at a temperature of  $\sim 360$  K, thus resulting in the  $\text{MnO}_6$  octahedra becoming briefly regular and isotropic before they distort again at higher temperatures.

We finally note the difference between the apical and equatorial Mn-O bond lengths [ $\Delta(\text{Mn-O})$ ] for the A-site disordered  $\text{La}_{0.5}\text{Ba}_{0.5}\text{MnO}_3$  phase to vary from 0 to  $0.003$  Å between 300 K and 10 K, respectively. In previous work,<sup>17</sup> we observed a more significant bond divergence for A-site ordered  $\text{La}_{0.5}\text{Ba}_{0.5}\text{MnO}_3$  with  $\Delta(\text{Mn-O})$  changing from

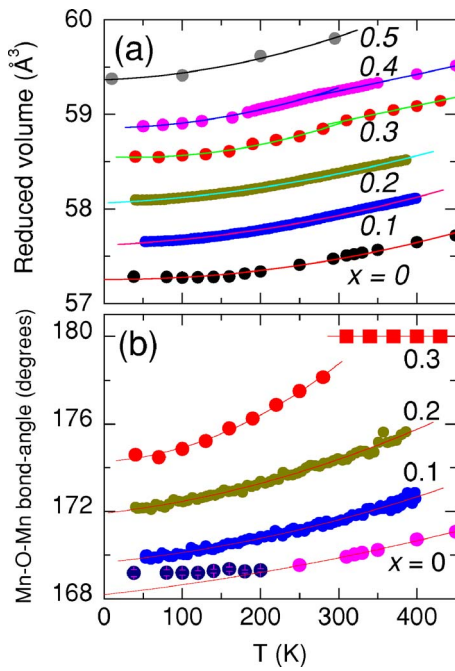


FIG. 8. (Color online) (a) Temperature-dependent (reduced) unit cell volume increasing regularly in magnitude as a function of increasing Ba content. (b) Mn-O-Mn bond angle as a function of temperature and Ba content.

0.005 to 0.055 Å between 300 K and 10 K, respectively. Nonetheless, the average  $\langle \text{Mn-O} \rangle$  bonds for both the A-site ordered and disordered  $\text{La}_{0.5}\text{Ba}_{0.5}\text{MnO}_3$  phases are almost identical at all temperatures (1.9544 and 1.9574 Å at room temperature, respectively) yet  $T_C$  is enhanced by as much as 80 K for the A-site ordered material. Consequently, the  $T_C$  enhancement for the A-site ordered phase could be directly attributed to the ordering of the A-site ions on alternate layers and the effects of ordering on the electronic band structure.

#### Effects of ionic size and size variance

We now turn our attention to the investigation of the ionic size and size variance effects on the magnetic and structural properties of  $\text{La}_{0.5}\text{Sr}_{0.5-x}\text{Ba}_x\text{MnO}_3$ . In this section, we will compare our results with those reported for other similar systems [e.g.,  $\text{La}_{0.5}\text{Ca}_{0.5-x}\text{A}_x\text{MnO}_3$  ( $A=\text{Sr}, \text{Ba}$ ), etc.] and exam-

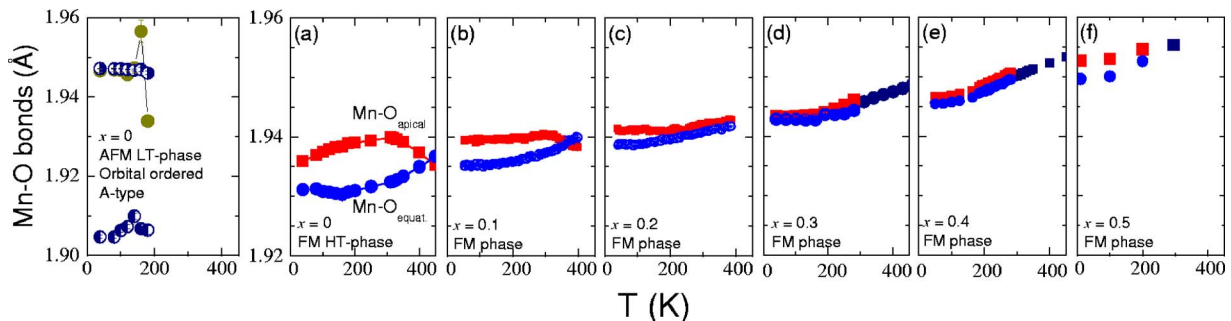


FIG. 9. (Color online) Temperature dependence of Mn-O bond lengths.

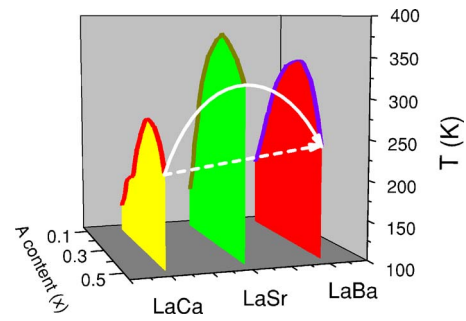


FIG. 10. (Color online)  $\text{La}_{1-x}\text{A}_x\text{MnO}_3$  phase diagrams ( $A = \text{Ca}, \text{Sr}, \text{Ba}$  and  $0.1 \leq x \leq 0.5$ ). For simplicity, only the ferromagnetic transitions are shown. The arrows in the figure show the two possible substitution paths (see text for more details) and the corresponding expected  $T_C$  behavior.

ine the properties of materials obtained with substitutions carried out according to two possible paths. Along the first path, Ca is substituted with Sr until all Ca ions have been substituted (i.e., resulting in  $\text{La}_{0.5}\text{Sr}_{0.5}\text{MnO}_3$ ) followed by the substitution of Ba with Sr until all Sr ions have been substituted, thus ending up with  $\text{La}_{0.5}\text{Ba}_{0.5}\text{MnO}_3$ . The second path involves the direct substitution of Ca ions with the larger Ba ions until all Ca ions have been replaced, thus resulting in  $\text{La}_{0.5}\text{Ba}_{0.5}\text{MnO}_3$ . The two substitution paths are better visualized by tracing the arrows shown in Fig. 10 between the  $\text{La}_{1-x}\text{Ca}_x\text{MnO}_3$ ,  $\text{La}_{1-x}\text{Sr}_x\text{MnO}_3$ , and  $\text{La}_{1-x}\text{Ba}_x\text{MnO}_3$  phase diagrams.

At this point, it is important to note that in this paper we will use A-site ionic sizes that we previously determined from precise neutron diffraction measurements of internal structural parameters and various A-O bond lengths in the manganites.<sup>4,7,15,16</sup> In these references, we demonstrate that the experimental ionic sizes of La (1.365 Å), Ca (1.24 Å), Sr (1.291 Å), and Ba (1.38 Å) in the perovskite manganites are significantly different from the calculated ionic sizes reported by Shannon (ionic sizes obtained by subtracting the six-coordinated oxygen ionic size from the A-O bond lengths). Acknowledging this discrepancy, researchers have frequently been using ionic sizes that correspond to nine coordinated A-site ions instead of the actual twelve coordinated ionic sizes. In Fig. 11, we plot the average (La, Sr, Ba)-O bond lengths as a function of Ba content for the current system as obtained from the Rietveld refinements (closed circles). Bond lengths calculated using our ionic size values

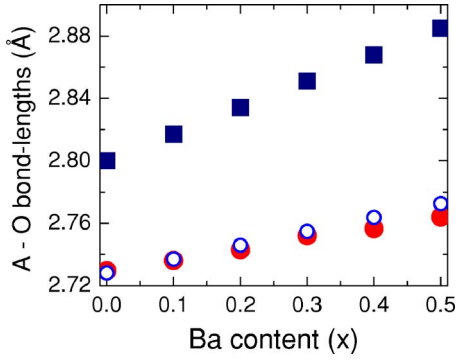


FIG. 11. (Color online)  $A$ - $O$  measured bond lengths (closed circles), calculated using our determined ionic sizes (open circles) and using Shannon's ionic sizes (closed squares). See text for more details.

are also shown (open circles) together with those calculated using Shannon's values (closed squares). The figure clearly demonstrates the validity of our experimental  $A$ -site sizes and the inadequate use of Shannon's ionic sizes for the manganites. For  $x > 0.3$ , the slightly overestimated bond lengths are due to strain effects in the cubic materials for which the Mn-O bonds are stretched and  $A$ - $O$  bonds are compressed.

In Tables III and IV,  $T_C$  values are listed for all members of our  $\text{La}_{0.5}\text{Sr}_{0.5-x}\text{Ba}_x\text{MnO}_3$  series together with those of  $\text{La}_{0.5}\text{Ca}_{0.5-x}\text{Sr}_x\text{MnO}_3$  and  $\text{La}_{0.5}\text{Ca}_{0.5-x}\text{Ba}_x\text{MnO}_3$  as extracted from the literature.<sup>11,21,22,25,32</sup> Consistent  $T_C$  values were found for most members of the  $\text{La}_{0.5}\text{Ca}_{0.5-x}\text{Sr}_x\text{MnO}_3$  series. Unfortunately, only a few papers reported on the characteristics and properties of  $\text{La}_{0.5}\text{Ca}_{0.5-x}\text{Ba}_x\text{MnO}_3$ .<sup>22,24,25,32,34</sup> Nevertheless, we concluded the following: (1) the synthesis of single phase  $\text{La}_{0.5}\text{Ca}_{0.5-x}\text{Ba}_x\text{MnO}_3$  is difficult but feasible under special synthesis conditions for low Ba concentrations, (2) most published work shows that the  $x \geq 0.3$  samples contain various amounts of a hexagonal  $\text{BaMnO}_3$  impurity phase that result in La-rich off-stoichiometric compositions, and (3)  $T_C$  increases very slightly and show essentially a "constant"

TABLE III.  $A$ -site average ionic size, size variance, and  $T_C$  for  $\text{La}_{0.5}\text{Ca}_{0.5-x}\text{Sr}_x\text{MnO}_3$  (Refs. 11–21) and  $\text{La}_{0.5}\text{Sr}_{0.5-x}\text{Ba}_x\text{MnO}_3$  (this work).

A-site composition	$\langle r_A \rangle$ (Å)	$\sigma^2$	$T_C$ (K)
$\text{La}_{0.5}\text{Ca}_{0.5}$	1.3	0.0036	228
$\text{La}_{0.5}\text{Ca}_{0.4}\text{Sr}_{0.1}$	1.305	0.00323	250
$\text{La}_{0.5}\text{Ca}_{0.3}\text{Sr}_{0.2}$	1.31	0.0028	270
$\text{La}_{0.5}\text{Ca}_{0.2}\text{Sr}_{0.3}$	1.315	0.00233	287
$\text{La}_{0.5}\text{Ca}_{0.15}\text{Sr}_{0.35}$	1.3175	0.00207	290
$\text{La}_{0.5}\text{Ca}_{0.1}\text{Sr}_{0.4}$	1.32	0.0018	300
$\text{La}_{0.5}\text{Sr}_{0.5}$	1.325	0.00123	316
$\text{La}_{0.5}\text{Sr}_{0.4}\text{Ba}_{0.1}$	1.334	0.00132	310
$\text{La}_{0.5}\text{Sr}_{0.3}\text{Ba}_{0.2}$	1.343	0.00126	300
$\text{La}_{0.5}\text{Sr}_{0.2}\text{Ba}_{0.3}$	1.352	0.00104	288
$\text{La}_{0.5}\text{Sr}_{0.1}\text{Ba}_{0.4}$	1.361	0.00065	268
$\text{La}_{0.5}\text{Ba}_{0.5}$	1.37	0.0001	240

TABLE IV.  $A$ -site average ionic size, size variance, and  $T_C$  for  $\text{La}_{0.5}\text{Ca}_{0.5-x}\text{Ba}_x\text{MnO}_3$ .  $T_C$  values were extracted from Refs. 22–25.

A-site composition	$\langle r_A \rangle$ (Å)	$\sigma^2$	$T_C$ (K)
$\text{La}_{0.5}\text{Ca}_{0.5}$	1.3	0.0036	228
$\text{La}_{0.5}\text{Ca}_{0.4}\text{Ba}_{0.1}$	1.314	0.00368	230
$\text{La}_{0.5}\text{Ca}_{0.3}\text{Ba}_{0.2}$	1.328	0.00338	225
$\text{La}_{0.5}\text{Ca}_{0.2}\text{Ba}_{0.3}$	1.342	0.00268	230
$\text{La}_{0.5}\text{Ca}_{0.1}\text{Ba}_{0.4}$	1.356	0.00158	290
$\text{La}_{0.5}\text{Ba}_{0.5}$ (this work)	1.37	0.0001	240

character (within  $\pm 10$  K) except for the  $x=0.4$  sample with a  $T_C$  as high as 290 K. The off-stoichiometry of this impurity-containing sample could explain its high  $T_C$ , which is in agreement with similar  $T_C$ 's typically observed for  $\text{La}_{1-x}\text{Ba}_x\text{MnO}_3$  with  $x$  contents slightly less than 0.5.<sup>8</sup>

The dependence of  $T_C$  on the average  $A$ -site ionic size,  $\langle r_A \rangle$ , for  $\text{La}_{0.5}\text{Ca}_{0.5-x}\text{Sr}_x\text{MnO}_3$  and  $\text{La}_{0.5}\text{Sr}_{0.5-x}\text{Ba}_x\text{MnO}_3$  reveals the presence of a  $T_C$  maximum at  $\text{La}_{0.5}\text{Sr}_{0.5}\text{MnO}_3$  as displayed in Fig. 12 in remarkable agreement with the first path arrow shown in Fig. 10. Interestingly, the  $T_C$  behavior for the current system is very similar to the previously observed  $T_N$  dependence on  $\langle r_A \rangle$  for  $\text{Sr}_{1-x}\text{A}_x\text{MnO}_3$  ( $A = \text{Ca}, \text{Ba}$ ).<sup>4</sup> In fact, in both systems, the Mn oxidation state remains unaffected by the isovalent substitutions carried out at the  $A$ -sites and both the  $T_C$  and  $T_N$  increase from a minimum for  $A = \text{Ca}$  [i.e.,  $\text{CaMnO}_3$  or  $\text{La}_{0.5}\text{Ca}_{0.5}\text{MnO}_3$ ] to a maximum for  $A = \text{Sr}$  [i.e.,  $\text{SrMnO}_3$  or  $\text{La}_{0.5}\text{Sr}_{0.5}\text{MnO}_3$ ]. In  $\text{Sr}_{1-x}\text{A}_x\text{MnO}_3$ , the increasing and decreasing properties of  $T_N$  correlate well with the average structural distortion variables  $\cos^2 \theta$  (directly related to  $\langle r_A \rangle$ ) (Refs. 2 and 35) and size variance  $\sigma^2$ , where  $\theta$  represents the average equatorial and apical Mn-O-Mn buckling angle and  $\sigma^2$  has previously<sup>4</sup> been shown to correlate with the refined Debye-Waller factor for oxygen which models the local distortions from the average structure. It should be stressed, however, that these correla-

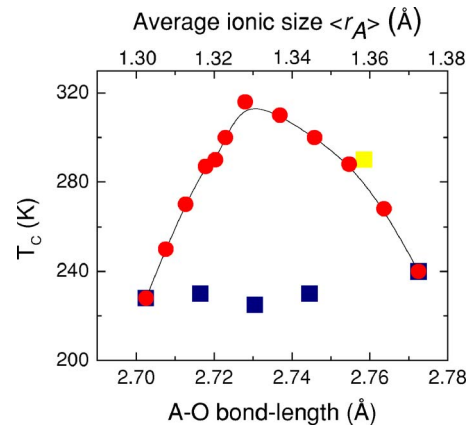


FIG. 12. (Color online)  $T_C$  as a function of  $A$ - $O$  bond length or average ionic size  $\langle r_A \rangle$ . The  $T_C$  dependence on  $A$ - $O$  ( $\langle r_A \rangle$ ) looks like an inverted parabola for the two series of the first substitution path (see Fig. 10) (i.e.,  $\text{La}_{0.5}\text{Ca}_{0.5-x}\text{Sr}_x\text{MnO}_3$  and  $\text{La}_{0.5}\text{Sr}_{0.5-x}\text{Ba}_x\text{MnO}_3$ ). A nearly constant (slight increase)  $T_C$  vs  $A$ - $O$  ( $\langle r_A \rangle$ ) behavior is observed for the  $\text{La}_{0.5}\text{Ca}_{0.5-x}\text{Ba}_x\text{MnO}_3$  series.

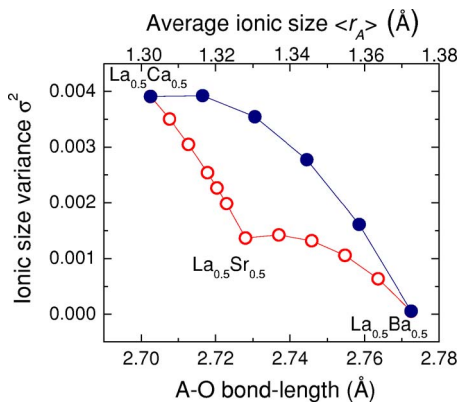


FIG. 13. (Color online) Size variance  $\sigma^2$  as a function of A-O ( $\langle r_A \rangle$ ) calculated for the two substitution paths discussed in the text and illustrated in Fig. 10.

tions are only valid if accurate Mn-O-Mn bond angles and Mn-O bond lengths obtained from NPD were used.

In the present system, the left part of the inverted parabola can be easily understood in terms of increasing ionic size (i.e., reduced buckling angle  $\theta$ ) and decreasing ionic size variance ( $\sigma^2$ ) upon increasing the Sr content at the  $\text{La}_{0.5}\text{Ca}_{0.5-x}\text{Sr}_x$  sites.<sup>2,4</sup> On the other hand, in  $\text{La}_{0.5}\text{Sr}_{0.5-x}\text{Ba}_x\text{MnO}_3$  (the right side of the parabola), Ba (ionic radius = 1.38 Å) substitution on Sr (ionic radius = 1.291 Å) sites initially causes  $\sigma^2$  to increase very slightly (for  $x \leq 0.2$ ) before rapidly decreasing for higher Ba contents, see Fig. 13. As can be seen in the figure, the combination of  $\langle r_A \rangle$  and  $\sigma^2$  in this composition range is actually favorable to increasing  $T_C$  and cannot explain the observed  $T_C$  reduction. However, the nearly constant behavior of  $\sigma^2$ , for  $x \leq 0.2$ , coupled with reduced  $T_C$  suggests the presence of (an) additional variable(s) that negatively affect(s) the  $T_C$ . Similar decreases in  $T_C$  near the cubic structural symmetry have been previously observed in  $\text{La}_{0.6}\text{Sr}_{0.4-x}\text{Ba}_x\text{MnO}_3$  and rationalized in terms of either increasing ionic size variance<sup>9</sup> or increasing Mn-O bond lengths that cause the bandwidth  $W \sim \cos \omega / [d_{\text{Mn-O}}]^{3.5}$  (where  $\omega = (180^\circ - \theta)/2$  and  $\theta$  is the Mn-O-Mn bond angle) to decrease in the double-exchange model of ferromagnetism in manganites.<sup>10</sup> As shown above, the accurately measured bond lengths demonstrate that the  $T_C$  behavior cannot be explained in terms of increasing ionic size variance near the cubic regime. While the full explanation of the observed  $T_C$  reduction should require more studies, we speculate at this time that at least two additional mechanisms could be invoked when the crystal structure is cubic or nearly cubic. In this paper and in previous work,<sup>36</sup> we have demonstrated that the incompatibility of ferromagnetism with the cubic symmetry is relieved by the presence of subtle structural distortions (according to Rodriguez-Martinez and Attfield's model, cubic symmetries should lead to maximum  $T_C$ 's when the variance of sizes is small. Note, however, that in the  $\text{Sr}_{1-x}\text{A}_x\text{MnO}_3$  system,<sup>4</sup> the maximum  $T_N$  is indeed observed for the cubic phase since there is no competition between antiferromagnetism and strains). These dis-

tortions could cause a variance in either the bond angles or bond lengths on the local length-scale, thus, resulting in suppressing  $T_C$  through a competitive mechanism between ferromagnetism and strains. A second mechanism could arise from the presence of Mn-O bonds that are stretched beyond their equilibrium values even in the noncubic phase. Fractions of such bonds would be present because the equilibrium Mn-O bonds are smaller than the longest  $A-O/\sqrt{2}$  bonds (i.e., the Ba-O bonds) even if the average structure is not cubic, i.e., when the tolerance factor is still smaller than 1 or the average bond angle Mn-O-Mn  $< 180^\circ$ . As the bandwidth equation (W) shows, these bonds would cause a very strong and nonlinear decrease of  $T_C$  that is not modeled by the variance of sizes  $\sigma^2$ . The presence of stretched out Mn-O bonds caused by the substitutions of larger Ba ions for Sr in the lattice as the materials become cubic indicates the development of considerable internal strains that cause the lowering of  $T_C$ .

As for the second substitution path, it is interesting to note that  $T_C$  appears independent of any of the above-mentioned variables (see Fig. 10). We speculate that the positive effects that result from the favorable change in  $\langle r_A \rangle$  would be almost completely compensated by the negative effects of  $\sigma^2$  and other local distortion variables. As such,  $T_C$  increases only slightly.

## CONCLUSIONS

We have investigated the effects of isovalent substitutions on the properties of  $\text{La}_{0.5}\text{Sr}_{0.5-x}\text{Ba}_x\text{Mn}^{(3.5+)}\text{O}_3$  materials. Using neutron powder diffraction, we showed that low Ba substitution levels result in the suppression of a previously observed low-temperature orbital-ordered antiferromagnetic phase in  $\text{La}_{0.5}\text{Sr}_{0.5}\text{MnO}_3$ . Further, we demonstrated that nuclear and magnetic structural transitions from  $I4/mcm/I4/mc'm'$  to  $Pm\bar{3}m/P4/mmm'$  take place for  $x \sim 0.3$ . It is particularly important to point out the tetragonal symmetry of  $\text{La}_{0.5}\text{Ba}_{0.5}\text{MnO}_3$  in its ferromagnetic state, as required by the ferromagnetic alignment of the Mn spins and structural symmetry considerations.

Finally, our results combined with data published in the literature demonstrate the existence of at least two substitution paths that yield different  $T_C$ 's and behaviors as a function of ionic size  $\langle r_A \rangle$ . We showed the dependence of  $T_C$  on  $\langle r_A \rangle$  to look like an inverted parabola for the  $\text{La}_{0.5}\text{Ca}_{0.5}\text{MnO}_3 \rightarrow \text{La}_{0.5}\text{Sr}_{0.5}\text{MnO}_3 \rightarrow \text{La}_{0.5}\text{Ba}_{0.5}\text{MnO}_3$  substitution path and to remain nearly constant for the alternate  $\text{La}_{0.5}\text{Ca}_{0.5}\text{MnO}_3 \rightarrow \text{La}_{0.5}\text{Ba}_{0.5}\text{MnO}_3$  path, in good agreement with relationships expected from the magnetic phase diagrams.

## ACKNOWLEDGMENTS

Work at NIU was supported by the NSF Grant No. DMR-0302617 and the U.S. Department of Education. At ANL, this work was supported by the U.S. Department of Energy, Office of Science, under Contract No. W-31-109-ENG-38.

\*Deceased.

- <sup>1</sup>P. G. Radaelli, D. E. Cox, M. Marezio, and S. W. Cheong, *Phys. Rev. B* **55**, 3015 (1997).
- <sup>2</sup>L. M. Rodriguez-Martinez and J. P. Attfield, *Phys. Rev. B* **54**, R15 622 (1996).
- <sup>3</sup>L. M. Rodriguez-Martinez and J. P. Attfield, *Phys. Rev. B* **58**, 2426 (1998).
- <sup>4</sup>O. Chmaissem, B. Dabrowski, S. Kolesnik, J. Mais, D. E. Brown, R. Kruk, P. Prior, B. Pyles, and J. D. Jorgensen, *Phys. Rev. B* **64**, 134412 (2001).
- <sup>5</sup>G. Q. Gong, C. Canedy, G. Xiao, J. Z. Sun, A. Gupta, and W. J. Gallagher, *Appl. Phys. Lett.* **67**, 1783 (1995).
- <sup>6</sup>C. H. Chen and S.-W. Cheong, *Phys. Rev. Lett.* **76**, 4042 (1996).
- <sup>7</sup>O. Chmaissem, B. Dabrowski, S. Kolesnik, J. Mais, J. D. Jorgensen, and S. Short, *Phys. Rev. B* **67**, 094431 (2003).
- <sup>8</sup>B. Raveau, C. Martin, A. Maignan, and M. Hervieu, *J. Phys.: Condens. Matter* **14**, 1297 (2002).
- <sup>9</sup>N. Abdelmoula, E. Dhahri, K. Guidara, and J. C. Joubert, *Phase Transitions* **69**, 215 (1999).
- <sup>10</sup>C. H. Shen, C. C. Chen, R. S. Liu, R. Gundakaram, S. F. Hu, and J. M. Chen, *J. Solid State Chem.* **156**, 117 (2001).
- <sup>11</sup>F. Damay, C. Martin, A. Maignan, and B. Raveau, *J. Appl. Phys.* **82**, 6181 (1997).
- <sup>12</sup>C. Autret, C. Martin, M. Hervieu, A. Maignan, B. Raveau, G. Andre, F. Bouree, and Z. Jirak, *Chem. Mater.* **15**, 1886 (2003).
- <sup>13</sup>E. Suard, F. Fauth, C. Martin, A. Maignan, F. Millange, and L. Keller, *J. Magn. Magn. Mater.* **264**, 221 (2003).
- <sup>14</sup>R. D. Shannon, *Acta Crystallogr., Sect. A: Cryst. Phys., Diffr., Theor. Gen. Crystallogr.* **32**, 751 (1976).
- <sup>15</sup>B. Dabrowski, O. Chmaissem, J. Mais, S. Kolesnik, J. D. Jorgensen, and S. Short, *J. Solid State Chem.* **170**, 154 (2003).
- <sup>16</sup>B. Dabrowski, S. Kolesnik, A. Baszczuk, O. Chmaissem, T. Maxwell, and J. Mais, *J. Solid State Chem.* **178**, 629 (2005).
- <sup>17</sup>O. Chmaissem, B. Dabrowski, S. Kolesnik, J. Mais, J. D. Jorgensen, S. Short, C. E. Botez, and P. W. Stephens, *Phys. Rev. B* **72**, 104426 (2005).
- <sup>18</sup>J. D. Jorgensen, J. J. Faber, J. M. Carpenter, R. K. Crawford, J. R. Haumann, R. L. Hitterman, R. Kleb, G. E. Ostrowski, F. J. Rotella, and T. G. Worlton, *J. Appl. Crystallogr.* **22**, 321 (1989).
- <sup>19</sup>A. C. Larson and R. B. von Dreele, Los Alamos National Laboratory Report No. LAUR 86-748, 2000 (unpublished).
- <sup>20</sup>B. H. Toby, *J. Appl. Crystallogr.* **34**, 210 (2001).
- <sup>21</sup>A. Sundaresan, P. L. Paulose, R. Mallik, and E. V. Sampathkumaran, *Phys. Rev. B* **57**, 2690 (1998).
- <sup>22</sup>H. Wakai, *J. Phys.: Condens. Matter* **13**, 1627 (2001).
- <sup>23</sup>Y. Jiang and S. L. Yuan, *Solid State Commun.* **120**, 185 (2001).
- <sup>24</sup>S. L. Yuan, F. Tu, Y. P. Yang, X. Y. Zeng, G. Q. Zhang, G. Peng, J. Liu, Y. Jiang, Z. Y. Li, C. S. Xiong, W. H. Xiong, and C. Q. Tang, *Phys. Status Solidi A* **185**, 391 (2001).
- <sup>25</sup>R. Mallik, E. S. Reddy, P. L. Paulose, S. Majumdar, and E. V. Sampathkumaran, *J. Phys.: Condens. Matter* **11**, 4179 (1999).
- <sup>26</sup>J. R. Sun, Z. X. Liu, C. F. Yeung, H. N. Chan, H. K. Wong, R. W. Li, and B. G. Shen, *J. Appl. Phys.* **91**, 3139 (2002).
- <sup>27</sup>S. V. Trukhanov, *J. Mater. Chem.* **13**, 347 (2003).
- <sup>28</sup>S. V. Trukhanov, L. S. Lobanovski, M. V. Bushinsky, I. O. Troyanchuk, and H. Szymczak, *J. Phys.: Condens. Matter* **15**, 1783 (2003).
- <sup>29</sup>I. O. Troyanchuk, S. V. Trukhanov, H. Szymczak, and K. Baerner, *J. Phys.: Condens. Matter* **12**, L155 (2000).
- <sup>30</sup>C. Roy and R. C. Budhani, *J. Appl. Phys.* **85**, 3124 (1999).
- <sup>31</sup>P. G. Radaelli, M. Marezio, H. Y. Hwang, and S.-W. Cheong, *J. Solid State Chem.* **122**, 444 (1996).
- <sup>32</sup>A. Barnabe, F. Millange, A. Maignan, M. Hervieu, B. Raveau, G. Van Tendeloo, and P. Laffez, *Chem. Mater.* **10**, 252 (1998).
- <sup>33</sup>F. Millange, V. Caignaert, B. Domenges, B. Raveau, and E. Suard, *Chem. Mater.* **10**, 1974 (1998).
- <sup>34</sup>V. N. Smolyaninova, S. E. Lofland, C. Hill, R. C. Budhani, Z. Serpil Gonen, B. W. Eichhorn, and R. L. Greene, *J. Magn. Magn. Mater.* **248**, 348 (2002).
- <sup>35</sup>J. P. Attfield, A. L. Kharlanov, and J. A. McAllister, *Nature (London)* **394**, 157 (1998).
- <sup>36</sup>O. Chmaissem, B. Dabrowski, S. Kolesnik, S. Short, and J. D. Jorgensen, *Phys. Rev. B* **71**, 174421 (2005).